

Variable-Length Wideband CSI Feedback via Loewner Interpolation and Deep Learning

Meilin Li, Wei Xu, Zhixiang Hu and An Liu, *Senior Member, IEEE*

Abstract—In this paper, we propose a variable-length wideband channel state information (CSI) feedback scheme for Frequency Division Duplex (FDD) massive multiple-input multiple-output (MIMO) systems in U6G band (6425MHz-7125MHz). Existing compressive sensing (CS)-based and deep learning (DL)-based schemes preprocess the channel by truncating it in the angular-delay domain. However, the energy leakage effect caused by the Discrete Fourier Transform (DFT) basis will be more serious and leads to a bottleneck in recovery accuracy when applied to wideband channels such as those in U6G. To solve this problem, we introduce the Loewner Interpolation (LI) framework which generates a set of dynamic bases based on the current CSI matrix, enabling highly efficient compression in the frequency domain. Then, the LI basis is further compressed in the spatial domain through a neural network. To achieve a flexible trade-off between feedback overhead and recovery accuracy, we design a rateless auto-encoder trained with tail dropout and a multi-objective learning schedule, supporting variable-length feedback with a singular model. Meanwhile, the codewords are ranked by importance, ensuring that the base station (BS) can still maintain acceptable reconstruction performance under limited feedback with tail erasures. Furthermore, an adaptive quantization strategy is developed for the feedback framework to enhance robustness. Simulation results demonstrate that the proposed scheme could achieve higher CSI feedback accuracy with less or equal feedback overhead, and improve spectral efficiency compared with baseline schemes.

Index Terms—CSI Feedback, Loewner Interpolation, Model Order Reduction, massive MIMO, deep learning

I. INTRODUCTION

Massive multiple-input multiple-output (MIMO) technology is a key technology for enhancing system capacity and spectral efficiency in 5G and beyond systems [1] [2]. For Frequency Division Duplex (FDD) systems, the reciprocity between the uplink channel and the downlink channel is weak. The base station (BS) obtains accurate downlink channel state information (CSI) by sending downlink pilots and receiving feedback from the user equipment (UE). In 2022, the 3rd Generation Partnership Project (3GPP) officially authorized the U6G spectrum (6425MHz~7125MHz), marking this band as a potential spectrum hotspot in the next generation communication systems. With such huge bandwidth and the increasing number of transmit antennas, the dimension of the CSI matrix significantly increases and leads to a large feedback overhead [3] [4]. To leverage the advantages of massive MIMO systems in U6G band, ensuring high-precision CSI feedback while controlling the feedback overhead becomes a key technical challenge.

A. Related Works

For CSI feedback in FDD massive MIMO systems, a wide range of approaches have been proposed. Generally, these

methods can be classified into three categories: codebook-based feedback schemes, compressed sensing (CS)-based feedback schemes and deep learning (DL)-based feedback schemes.

For codebook-based CSI feedback, some works design codebooks by exploiting channel sparsity in the angular and/or delay domains [5]–[7]. For instance, [5] proposed a subspace codebook that adapts to the angle of departure (AoD). However, it relies on the assumption that the AoD support remains stable over a relatively long coherence interval. 3GPP Release-16 (R16) proposed the Enhanced Type II (eType II) codebook [6], which leverages the sparsity in the angular and delay domains via a Discrete Fourier Transform (DFT) basis. However, the eType II codebook in R16 is constrained by both the number of antenna ports (maximum 32) and the supported bandwidth. For massive MIMO systems envisioned for U6G, these limitations, together with the energy leakage inherent to the fixed DFT basis, lead to notable deterioration in CSI reconstruction accuracy. Some subsequent works have focused on designing precoders to increase channel sparsity. [7] proposed an eigenvector-based precoder that leverages partial angle-delay reciprocity between uplink and downlink channels. This approach, however, requires precise channel statistics, which are often difficult to obtain in practice.

For CS-based CSI feedback, the inherent correlation structure within the channel matrix enables a compact and sparse representation in a suitable transform domain. CS theory thus provides an efficient mechanism for CSI feedback by formulating it as a sparse signal recovery problem. Conventional CS algorithms like Least Absolute Shrinkage and Selection Operator (LASSO) and Approximate Message Passing (AMP) are constrained by their reliance on simple sparsity assumptions. To overcome these limitations, more advanced CS-based approaches, including BM3D-AMP [8] and TVAL3 [9], have been developed to exploit richer prior models. Also, some studies further exploit correlations of the channels across different domains to design CS-based CSI feedback schemes. For example, [10] proposed a hybrid adaptive feedback scheme leveraging the optimality of the Karhunen-Loeve Transform (KLT) and the sparsity in the spatial and frequency domains arising from spatially correlated antenna arrays. In [11], a partial channel support information (P-CSPI)-aided burst LASSO algorithm was developed to utilize the temporal correlation of the channel support, thereby reducing pilot and feedback overhead. Although CS-based feedback methods have a solid theoretical foundation, most of them rely on iterative reconstruction which leads to high computational complexity and struggle to achieve higher recovery accuracy.

3GPP R18/19 further introduces artificial intelligence (AI) to CSI feedback as a promising key technology. DL-based

CSI feedback schemes treat downlink CSI as an image and aim to reconstruct the original image from its latent space representation. Many studies [12]–[15] have achieved high reconstruction accuracy by refining the architecture of the auto-encoder. However, these methods typically rely on DFT and truncation as preprocessing steps of the original channel matrix. In wideband scenarios, the energy leakage problem caused by DFT is more serious. A large truncation ratio results in significant precision loss before network compression, forming a bottleneck in reconstruction accuracy, while a small truncation ratio significantly increases the computational complexity of the network. Furthermore, most of these approaches neglect the reconstruction error caused by codeword quantization and are limited to a single compression ratio (CR).

Several recent studies have attempted to overcome the aforementioned limitations by removing the dependency on DFT-based preprocessing and enabling multi-rate CSI feedback with codeword quantization. [16] proposed a compressive sampled CSI feedback method which combines sampling with neural networks. Instead of using the DFT basis, the compression in the frequency domain is achieved through a sampling network and an interpolation network. However, the application scenario for [16] is limited to narrowband scenarios, where the number of subcarriers used in simulation is relatively small. When extended to wideband channels with a significantly larger number of subcarriers, the computational complexity of the network increases sharply due to the higher dimension of the input tensor, potentially leading to increased training cost, longer inference time, and reduced practicality in U6G massive MIMO systems. In [17], multi-rate feedback with quantization is considered based on the proposed serial multiple-rate framework and parallel multiple-rate framework. However, the BS needs to deploy several pre-trained decoders according to the corresponding CRs and the length of the feedback codewords is still fixed. [18] proposed an integrated, bit-level feedback mechanism with variable-length feedback adaptability which takes the current CSI matrix directly as the input of the auto-encoder and arranges a large number of self-attention mechanisms [19] at the BS. Simulation results indicate that though a flexible trade-off between feedback overhead and accuracy has been achieved, the recovery accuracy of the CSI matrix is low and the computational complexity is higher than that of other convolutional neural networks (CNNs).

Although there is a large body of work on CSI feedback, most of these methods have one of the following drawbacks. First, they focus more on the CR and ignore the reconstruction error introduced by the quantization of the feedback codewords. Second, the CRs supported by these schemes are limited, and the length of the output codewords is still fixed which poses challenges for practical deployment in some scenarios such as *channels with tail erasures*¹. Third, they

¹A channel with tail erasures is suitable for the situation where the receiver effectively stops obtaining meaningful symbols after an unknown point in time. In this scenarios, only an initial portion of the codeword is reliably received, either due to abrupt link interruption or due to a system intentionally decoding [20].

preprocess the channel matrix with DFT and consider the reconstruction of the truncated sparse angular-delay channel $\tilde{\mathbf{H}} = f_{trun}(\mathbf{F}_d \mathbf{H} \mathbf{F}_a^H)$, where $f_{trun}(\cdot)$ denotes the truncation operator. Although some existing methods can achieve high-precision recovery of $\tilde{\mathbf{H}}$, the energy leakage problem caused by DFT and truncation in the wideband scenario is more serious, resulting in a reconstruction accuracy bottleneck induced by $f_{trun}(\cdot)$. In summary, achieving high-accuracy CSI feedback and a flexible trade-off between overhead and precision with quantization remains a key issue in massive MIMO systems applied to the U6G band.

B. Key Contributions

To address the issues mentioned above, this paper proposes a variable-length wideband CSI feedback based on Loewner Interpolation (LI) framework and DL. This paper substantially extends our prior work [21], where a preliminary LI-based compression scheme was introduced. In this paper, the framework is further generalized to the frequency domain and integrated with a rateless DL-based spatial compression architecture and a robust quantization strategy, providing a more comprehensive system framework. The main contributions of this paper are summarized as follows:

- LI-based compression in the frequency domain: Unlike most of the DL-based CSI feedback schemes preprocessing the CSI matrix with DFT and truncation, we introduce the LI framework to learn a set of effective bases from the current CSI matrix in a straightforward manner and ensure perfect recovery at sample points based on the system-theoretical methodology. Then the Model Order Reduction (MOR) in the LI framework helps to prevent the expansion of the parameters and achieve flexible compression in the frequency domain. As a result, we obtain a set of LI basis matrices $\{\mathbf{A}, \mathbf{B}, \mathbf{C}\}$ with simple structures. In particular, $\mathbf{A} \in \mathbb{C}^{r_f \times r_f}$ is a diagonal matrix with r_f denoting the order preserved in the frequency domain, and $\mathbf{B} \in \mathbb{C}^{r_f \times 2}$ is a low-dimensional matrix with the dimension 2 arising from the dual-polarized antenna configuration. Therefore, \mathbf{A} and \mathbf{B} only contain a small number of non-zero elements. On the other hand, $\mathbf{C} \in \mathbb{C}^{N_t \times r_f}$, where N_t represents the number of antennas, which is large for massive MIMO. As such, the feedback overhead of \mathbf{C} is dominated by the spatial dimension of \mathbf{C} .
- Rateless auto-encoder-based compression in the spatial domain: After obtaining the LI bases, we design a cascaded spatial compression scheme to further reduce the feedback overhead caused by the large spatial dimension of \mathbf{C} . Specifically, a matrix multiplication operator $\mathbf{F}(\cdot)$ is first designed to transform \mathbf{C} into another matrix $\mathbf{F}(\mathbf{C})$ to prevent the error amplification caused by algorithm cascading and sparsity enhancement. Then, the transformed matrix $\mathbf{F}(\mathbf{C})$ is fed into a rateless auto-encoder, which generates the corresponding codeword, denoted by \mathbf{v} . Furthermore, the rateless auto-encoder is trained with tail dropout and a multi-objective learning schedule to implement variable-length feedback of the codewords.

- Robust quantization algorithm for the overall framework: To account for quantization effects in the feedback scheme, we design different quantization schemes for all the codewords $\{\mathbf{A}, \mathbf{B}, \mathbf{v}\}$ respectively based on their numerical structures. Although the quantization bits of \mathbf{v} dominate the overall feedback overhead, the reconstruction error of \mathbf{H} is more sensitive to the reconstruction errors of $\{\mathbf{A}, \mathbf{B}\}$ than that of \mathbf{C} , which is primarily determined by the quantization error of \mathbf{v} and the CR of the auto-encoder. A slight refinement of the quantization bit allocation for $\{\mathbf{A}, \mathbf{B}\}$ can effectively enhance the robustness of the entire recovery process. Motivated by this observation, we develop an adaptive bit-allocation algorithm for $\{\mathbf{A}, \mathbf{B}\}$, achieving notable gains with only negligible additional feedback overhead. First, the algorithm computes the gradient matrix of the reconstruction error to identify potential low-accuracy recovery samples. Based on this information, the system proactively adjusts the quantization bit allocation at the UE to prevent the potential abnormal recovery at the BS. Simulation results demonstrate that the proposed algorithm significantly enhances robustness with a negligible overhead increase.

The rest of the paper is organized as follows. Section II presents the system model for the CSI feedback in FDD massive MIMO systems. In Section III, we introduce the LI framework for the CSI compression in the frequency domain. Then, the further spatial-domain compression based on the rateless auto-encoder is introduced in Section IV. The robust quantization algorithm, along with the summary of the overall framework, is presented in Section V. In Section VI, we provide simulation results to demonstrate the performance of the proposed scheme. Finally, we give the conclusion of the paper in Section VII.

In this paper, we adopt the following notational conventions: a is a scalar; \mathbf{a} is a vector; \mathbf{A} is a matrix. $(\cdot)^T$, $(\cdot)^H$, $(\cdot)^*$, $diag(\cdot)$, $\|\cdot\|_F$ and $Tr(\cdot)$ denote the transpose, conjugate transpose, conjugate, diagonal matrix, Frobenius norm and trace respectively. $\mathbb{C}^{a \times b}$ is a matrix space with a rows and b columns. $(\mathbf{A})_{i,j}$ denotes the element in the i -th row and the j -th column of the matrix \mathbf{A} and $(\mathbb{A})_{i,j}$ denotes the submatrix located at the i -th row and the j -th column of the block matrix \mathbb{A} . \mathbf{I}_N and $\mathbf{0}_N$ represent an $N \times N$ identity matrix and a $N \times N$ zero matrix. \triangleq refers to the definition symbol.

II. SYSTEM MODEL

We consider a FDD massive MIMO system where the BS is equipped with N_t antennas and each UE has N_r antennas. The downlink channel at a given subcarrier k is modeled as a complex matrix $\mathbf{H}_k \in \mathbb{C}^{N_r \times 2N_t}$, where $2N_t$ accounts for the dual-polarization configuration of the transmitting antennas. For a wideband orthogonal frequency division multiplexing (OFDM) system employing N_f subcarriers, the overall channel can be represented as a three-dimensional tensor:

$$\mathcal{H} = [\mathbf{H}_1, \mathbf{H}_2, \dots, \mathbf{H}_{N_f}] \in \mathbb{C}^{N_r \times 2N_t \times N_f}$$

For FDD systems, the BS obtains CSI by sending downlink pilots and receiving feedback from the UE. It is assumed that

the UE has obtained perfect CSI via pilot-based estimation and this work concentrates on the design of the feedback scheme.

In our proposed feedback scheme, compression and feedback are performed independently for each receiving antenna slice. Specifically, for the i -th receiving antenna, the UE applies a compression operator $\mathcal{F}(\cdot)$ to its corresponding channel slice $\mathcal{H}_{i,:,:} \in \mathbb{C}^{2N_t \times N_f}$, producing a low-dimensional compressed representation:

$$\mathbf{z}_i = \mathcal{F}(\mathcal{H}_{i,:,:}) \in \mathbb{C}^d$$

where $d \ll 2N_t N_f$ denotes the number of feedback complex numbers. The compressed CSI vector \mathbf{z}_i is then transmitted to the BS. At the BS, the received feedback is decoded using a reconstruction function $\mathcal{G}(\cdot)$ to obtain an estimate of the original channel slice:

$$\hat{\mathcal{H}}_{i,:,:} = \mathcal{G}(\mathbf{z}_i) \in \mathbb{C}^{2N_t \times N_f}$$

By processing all N_r slices in parallel, the BS reconstructs the full channel tensor as

$$\hat{\mathcal{H}} = [\hat{\mathcal{H}}_{1,:,:}, \hat{\mathcal{H}}_{2,:,:}, \dots, \hat{\mathcal{H}}_{N_r,:,:}] \in \mathbb{C}^{N_r \times 2N_t \times N_f}$$

With $\hat{\mathcal{H}}$, the BS can perform the Singular Value Decomposition (SVD)-based precoding to assist downlink communication [22].

Specifically, for the R -th layer (data stream), the precoder is chosen as the eigenvector $\mathbf{v}_{R,k}$ associated with the R -th largest eigenvalue of $\hat{\mathbf{H}}_k^H \hat{\mathbf{H}}_k$, where $\hat{\mathbf{H}}_k$ denotes the reconstructed channel. By collecting the eigenvectors across all N_f subbands, the precoding matrix \mathbf{W}_R for layer R can be formed as follows:

$$\mathbf{W}_R = [\mathbf{v}_{R,1}, \dots, \mathbf{v}_{R,N_f}] \in \mathbb{C}^{2N_t \times N_f}$$

III. LI-BASED COMPRESSION IN THE FREQUENCY DOMAIN

This section presents the LI-based compression in the frequency domain which consists of two steps. First, an LI-based CSI interpolation model inspired by the standard Loewner matrix approach to the generalized realization problem is developed. Then, we introduce the order reduction for the LI model, along with a structural simplification of the bases to further reduce the feedback overhead and facilitate the subsequent spatial compression.

A. LI-Based CSI Interpolation Model

The LI method establishes a direct connection between data-driven modeling and the state-space realization of linear time-invariant (LTI) systems from its frequency-domain sampling data and has been proved to be suitable for solving massive-port problems [23] [24] [25]. Specifically, given a set of frequency-domain samples

$$\{(s_i, \mathbf{H}(s_i)) : s_i \in \mathbb{R}, \mathbf{H}(s_i) \in \mathbb{C}^{m \times n}\} \quad (1)$$

from an unknown system, the Loewner framework can construct a system descriptor:

$$\Sigma \triangleq (\mathbf{E}, \mathbf{A}, \mathbf{B}, \mathbf{C}) \quad (2)$$

whose transfer function is as:

$$\mathbf{H}(s) = \mathbf{C}(s\mathbf{E} - \mathbf{A})^{-1} \mathbf{B} \quad (3)$$

Inspired by the success of the LI framework in solving system realization problems for dynamic systems, we extend this concept to the frequency-domain compression of the CSI matrix. This extension of the LI framework from LTI system modeling to the frequency-domain representation and compression of CSI matrices is conceptually sound. In both cases, the core task is to reconstruct or represent a parametric system from its frequency-sampled data, whether it be a classical state-space model or a high-dimensional wireless channel characterized by its CSI. By interpreting the CSI matrices as frequency-response data, the proposed method leverages the Loewner-based modeling mechanism to capture the underlying correlation in the frequency domain and obtain a compact representation. This analogy allows the CSI compression problem to be reformulated as a data-driven realization task, enabling accurate reconstruction at the receiver while significantly reducing feedback overhead.

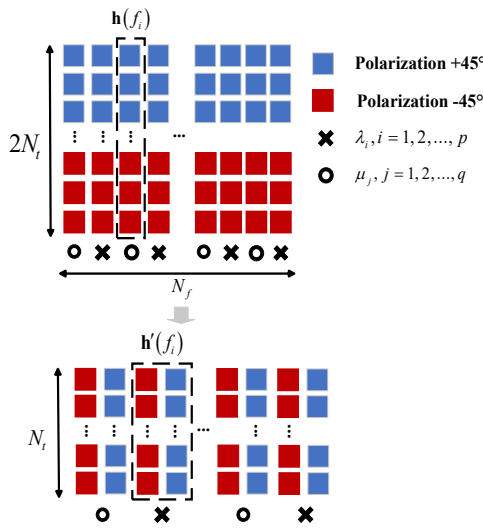


Fig. 1. The LI-based CSI interpolation model.

We regard the original CSI slice matrix $\mathbf{H} = \mathcal{H}_{i,:} \in \mathbb{C}^{2N_t \times N_f}$ as a set of samples, as defined in (4). Each column of $\mathbf{H} = \mathcal{H}_{i,:} \in \mathbb{C}^{2N_t \times N_f}$, indexed by f_i , represents a potential sample point with the corresponding column vector $\mathbf{h}(f_i) \in \mathbb{C}^{2N_t \times 1}$ serving as the associated sample value. The total number of sample points is denoted by N , which satisfies $1 \leq N \leq N_f$.

$$\mathcal{S} = \{f_i, \mathbf{h}(f_i), i = 1, 2, \dots, N\} \quad (4)$$

Each sample vector $\mathbf{h}(f_i) \in \mathbb{C}^{2N_t \times 1}$ is first reshaped to $\mathbf{h}'(f_i) \in \mathbb{C}^{N_t \times 2}$ according to the dual-polarization configuration of the transmitting antennas. The set \mathcal{S} is then divided into left and right interpolation subsets respectively, denoted as $\mathcal{S} = \mathcal{L} \cup \mathcal{M}$, leading to (5). The CSI interpolation model is constructed as illustrated in Fig. 1.

$$\begin{aligned} \mathcal{L} &= \{\lambda_i, \mathbf{h}'(\lambda_i), i = 1, 2, \dots, p\} \\ \mathcal{M} &= \{\mu_j, \mathbf{h}'(\mu_j), j = 1, 2, \dots, q\} \\ p + q &= N \end{aligned} \quad (5)$$

Using the left and right sampling sets, we construct the matrices \mathbf{V} and \mathbf{W} as follows (6):

$$\begin{aligned} \mathbf{V} &= \begin{bmatrix} \mathbf{h}'(\lambda_1) \\ \vdots \\ \mathbf{h}'(\lambda_p) \end{bmatrix} \in \mathbb{C}^{pN_t \times 2} \\ \mathbf{W} &= [\mathbf{h}'(\mu_1) \cdots \mathbf{h}'(\mu_q)] \in \mathbb{C}^{N_t \times 2q} \end{aligned} \quad (6)$$

Subsequently, the Loewner matrix $\mathbb{L} \in \mathbb{C}^{pN_t \times 2q}$ and the shifted Loewner matrix $\mathbb{L}_\sigma \in \mathbb{C}^{pN_t \times 2q}$ are formed as in (7) and (8). Both \mathbb{L} and \mathbb{L}_σ are block matrices of size $p \times q$, with each block being a $N_t \times 2$ submatrix:

$$\mathbb{L} = \left[\frac{\mathbf{h}'(\lambda_i) - \mathbf{h}'(\mu_j)}{\lambda_i - \mu_j} \right] \quad \forall i = 1, \dots, p \\ \forall j = 1, \dots, q \quad (7)$$

$$\mathbb{L}_\sigma = \left[\frac{\lambda_i \mathbf{h}'(\lambda_i) - \mu_j \mathbf{h}'(\mu_j)}{\lambda_i - \mu_j} \right] \quad \forall i = 1, \dots, p \\ \forall j = 1, \dots, q \quad (8)$$

According to the above definition, we have $(\mathbb{L}_\sigma - \lambda_i \mathbb{L})_{i,j} = \mathbf{h}'(\mu_j)$. Let $\mathbb{I}_i = [\mathbf{0} \cdots \mathbf{I}_i \in \mathbb{R}^{N_t \times N_t} \cdots \mathbf{0}] \in \mathbb{R}^{N_t \times pN_t}$ denote a $1 \times p$ block matrix where \mathbf{I}_i is an identity matrix at block i , we have $\mathbb{I}_i \mathbf{V} = \mathbf{h}'(\lambda_i)$ and $\mathbb{I}_i (\mathbb{L}_\sigma - \lambda_i \mathbb{L}) = \mathbf{W}$ for $\forall i = 1, \dots, p$. If $(\mathbb{L}_\sigma - \lambda_i \mathbb{L})$ is invertible, we have $\mathbf{h}'(\lambda_i) = \mathbb{I}_i \mathbf{V} = \mathbf{W} (\mathbb{L}_\sigma - \lambda_i \mathbb{L})^{-1} \mathbf{V}$. Consequently, the interpolation function is defined as (9):

$$\mathbf{g}(f) = \mathbf{W} (\mathbb{L}_\sigma - f \mathbb{L})^{-1} \mathbf{V} \in \mathbb{C}^{N_t \times 2} \quad (9)$$

The above proves that $\mathbf{g}(f)$ guarantees the perfect recovery at the sample point λ_i , i.e. $\mathbf{g}(\lambda_i) = \mathbf{h}'(\lambda_i)$, $i = 1, 2, \dots, p$. It is also easy to prove the perfect recovery for the other sample set: $\mathbf{g}(\mu_j) = \mathbf{h}'(\mu_j)$, $j = 1, 2, \dots, q$.

B. MOR for CSI Interpolation

To prevent an excessive feedback overhead, the MOR in the LI framework [26] is applied to $\{\mathbf{W}, \mathbf{V}, \mathbb{L}, \mathbb{L}_\sigma\}$. We first select a specific sample point λ_i and perform a SVD decomposition of $\mathbb{L}_\sigma - \lambda_i \mathbb{L}$ to obtain the corresponding projection matrices as (10). In practice, λ_i is chosen as the midpoint of the sampling set.

$$\begin{aligned} \mathbb{L}_\sigma - \lambda_i \mathbb{L} &= \mathbf{Y} \mathbf{\Sigma}_i \mathbf{X}^H \\ \mathbf{Y} &\in \mathbb{C}^{pN_t \times pN_t}, \mathbf{X} \in \mathbb{C}^{2q \times 2q}, \mathbf{\Sigma}_i \in \mathbb{C}^{pN_t \times 2q} \end{aligned} \quad (10)$$

After applying the projection matrices \mathbf{X}, \mathbf{Y} to $\{\mathbf{V}, \mathbf{W}, \mathbb{L}, \mathbb{L}_\sigma\}$, the interpolation function can be written as (11):

$$\begin{aligned} \mathbf{g}(f) &= (\mathbf{W} \mathbf{X}) \left(\mathbf{X}^H (\mathbb{L}_\sigma - f \mathbb{L})^{-1} \mathbf{Y} \right) (\mathbf{Y}^H \mathbf{V}) \\ &= (\mathbf{W} \mathbf{X}) (\mathbf{Y}^H \mathbb{L}_\sigma \mathbf{X} - f \mathbf{Y}^H \mathbb{L} \mathbf{X})^{-1} (\mathbf{Y}^H \mathbf{V}) \end{aligned} \quad (11)$$

If the projection matrices \mathbf{X} and \mathbf{Y} are suitably truncated, the feedback overhead can be reduced with only a slight decrease in the reconstruction accuracy. Specifically, we preserve the singular vectors corresponding to the largest r_f singular values of \mathbf{X}, \mathbf{Y} to construct the truncated matrices $\mathbf{X}_p, \mathbf{Y}_p$ where $r_f \ll \{pN_t, 2q\}$. This leads to the reduced-order interpolation function $\mathbf{g}(f) \approx \mathbf{C}_1 (f \mathbf{E}_1 - \mathbf{A}_1)^{-1} \mathbf{B}_1 \in \mathbb{C}^{N_t \times 2}$ where $\mathbf{A}_1, \mathbf{B}_1, \mathbf{C}_1, \mathbf{E}_1$ are defined in (12). The parameter r_f

represents the frequency order and is critical in the CSI interpolation model, striking a balance between recovery accuracy and feedback overhead.

$$\begin{cases} \mathbf{C}_1 \triangleq \mathbf{W} \mathbf{X}_p \in \mathbb{C}^{N_t \times r_f} \\ \mathbf{E}_1 \triangleq -\mathbf{Y}_p^H \mathbb{L} \mathbf{X}_p \in \mathbb{C}^{r_f \times r_f} \\ \mathbf{A}_1 \triangleq -\mathbf{Y}_p^H \mathbb{L}_\sigma \mathbf{X}_p \in \mathbb{C}^{r_f \times r_f} \\ \mathbf{B}_1 \triangleq \mathbf{Y}_p^H \mathbf{V} \in \mathbb{C}^{r_f \times 2} \end{cases} \quad (12)$$

Since the dimension of $\mathbf{A}_1, \mathbf{B}_1, \mathbf{C}_1, \mathbf{E}_1$ is still large, the feedback overhead can be further reduced by turning \mathbf{E}_1 to identity matrix with SVD $\mathbf{E}_1 = \mathbf{U}_e \mathbf{\Sigma}_e \mathbf{V}_e^H \in \mathbb{C}^{r_f \times r_f} * \mathbb{C}^{r_f \times r_f} * \mathbb{C}^{r_f \times r_f}$ and obtain (13).

$$\begin{cases} \mathbf{C}_2 \triangleq \mathbf{C}_1 \mathbf{V}_e \sqrt{\mathbf{\Sigma}_e^{-1}} \in \mathbb{C}^{N_t \times r_f} \\ \mathbf{A}_2 \triangleq \sqrt{\mathbf{\Sigma}_e^{-1}} \mathbf{U}_e^H \mathbf{A}_1 \mathbf{V}_e \sqrt{\mathbf{\Sigma}_e^{-1}} \in \mathbb{C}^{r_f \times r_f} \\ \mathbf{B}_2 \triangleq \sqrt{\mathbf{\Sigma}_e^{-1}} \mathbf{U}_e^H \mathbf{B}_1 \in \mathbb{C}^{r_f \times 2} \end{cases} \quad (13)$$

Then by diagonalizing \mathbf{A}_2 with SVD $\mathbf{A}_2 = \mathbf{U}_a \mathbf{\Sigma}_a \mathbf{U}_a^{-1} \in \mathbb{C}^{r_f \times r_f} * \mathbb{C}^{r_f \times r_f} * \mathbb{C}^{r_f \times r_f}$, the interpolation function can be further written as $\mathbf{g}(f) \approx \mathbf{C}_3 (f \mathbf{I} - \mathbf{A}_3)^{-1} \mathbf{B}_3$ where the new matrices $\{\mathbf{A}_3, \mathbf{B}_3, \mathbf{C}_3\}$, as expressed in (14), implicitly absorb the normalization and diagonalization transformations introduced in the previous steps.

$$\begin{cases} \mathbf{C}_3 \triangleq \mathbf{C}_2 \mathbf{U}_a \in \mathbb{C}^{N_t \times r_f} \\ \mathbf{A}_3 \triangleq \mathbf{\Sigma}_a \in \mathbb{C}^{r_f \times r_f} \\ \mathbf{B}_3 \triangleq \mathbf{U}_a^{-1} \mathbf{B}_2 \in \mathbb{C}^{r_f \times 2} \end{cases} \quad (14)$$

The dimension of matrices $\{\mathbf{A}_3, \mathbf{B}_3, \mathbf{C}_3\}$ is closely related to the order r_f where $r_f \ll \{pN_T, 2q\}$. Given any frequency index $f_p \in \{1, 2, \dots, N_f\}$, the BS can recover $\hat{\mathbf{H}}(f_p) \in \mathbb{C}^{N_t \times 2}$ with (15), which is the channel coefficients of the two polarization at subcarrier f_p .

$$\hat{\mathbf{H}}(f_p) = \mathbf{C}_3 (f_p \mathbf{I} - \mathbf{A}_3)^{-1} \mathbf{B}_3 \quad (15)$$

The proposed LI-based CSI compression scheme for the frequency domain is summarized in Fig. 2. By integrating the LI with MOR and further simplifying the basis, the high-dimensional CSI data are efficiently projected onto a compact and well-conditioned subspace and can be effectively represented by a set of descriptor $\{\mathbf{A}_3, \mathbf{B}_3, \mathbf{C}_3\}$. After the compression in the frequency domain, the feedback overhead (complex numbers) is $(3r_f + r_f \times N_t)$.

IV. RATELESS AUTO-ENCODER-BASED COMPRESSION IN THE SPATIAL DOMAIN

In this section, we introduce the rateless auto-encoder-based compression scheme for the spatial domain. We begin by introducing the general DL-based compression framework. Then, we develop a cascaded framework for the spatial domain compression architecture for \mathbf{C}_3 (one of the LI bases) which incorporates both the prevention of error amplification and sparsity enhancement. Finally, we introduce the implementation of the rateless auto-encoder which is called LI-MORNet that supports the variable-length feedback.

A. DL-Based Compression

We consider DL-based compression in the spatial domain by feeding the target matrix \mathbf{C} into an auto-encoder for further compression. Specifically, we aim to design an encoder:

$$\mathbf{v} = f_{en}(\mathbf{C}, \theta_{en}) \quad (16)$$

which maps $\mathbf{C} \in \mathbb{C}^{m \times n}$ into an M -dimensional real-vector codeword $\mathbf{v} \in \mathbb{R}^M$, where θ_{en} denotes the parameters of the encoder. The CR in the spatial domain is therefore defined as:

$$CR_s = \frac{M}{2mn} \quad (17)$$

In addition, we also design a decoder that reconstructs $\hat{\mathbf{C}}$ from the received codeword \mathbf{v} . Considering that the feedback is based on a quantized representation $\mathbf{v}_q = \mathcal{Q}(\mathbf{v})$, $\hat{\mathbf{C}}$ recovered at the BS is given by:

$$\hat{\mathbf{C}} = f_{de}(\mathcal{D}(\mathbf{v}_q), \varphi_{de}) \quad (18)$$

where $\mathcal{Q}(\cdot)$ and $\mathcal{D}(\cdot)$ denote the quantization and dequantization functions respectively. φ_{de} represents the parameters of the decoder, and \mathbf{v}_q is the quantized codeword.

B. Spatial Compression in the Cascaded Framework

After the compression in the frequency domain, we obtain $\{\mathbf{A}_3 \in \mathbb{C}^{r_f \times r_f}, \mathbf{B}_3 \in \mathbb{C}^{r_f \times 2}, \mathbf{C}_3 \in \mathbb{C}^{N_t \times r_f}\}$ where r_f denotes the preserved order and is typically small. Consequently, \mathbf{A}_3 and \mathbf{B}_3 are low-dimensional matrices. In contrast, $\mathbf{C}_3 \in \mathbb{C}^{N_t \times r_f}$ contains redundant information in the spatial domain with dimension N_t and thus can be further compressed.

However, directly feeding \mathbf{C}_3 into the auto-encoder leads to a critical issue: the reconstruction error $\Delta \mathbf{C}_3 = \hat{\mathbf{C}}_3 - \mathbf{C}_3 = f_{de}(f_{en}(\mathbf{C}_3, \theta_{en}), \varphi_{de}) - \mathbf{C}_3$ introduced by the auto-encoder will be subsequently amplified during the subsequent recovery in the frequency domain via the interpolation function. This error propagation arises from the cascaded structure of the two-step compression framework. In other words, $\Delta \mathbf{C}_3$ is not only preserved but further amplified when passed through the LI-based reconstruction module in the frequency domain. The following provides a detailed explanation of this error-amplification mechanism.

Consider the recovery interpolation function as (15) with the reconstructed $\hat{\mathbf{C}}_3$ while assuming $\{\mathbf{A}_3, \mathbf{B}_3\}$ are perfectly recovered. The reconstructed CSI $\hat{\mathbf{H}}_s$ at the sampled frequency index $\{f_1, f_2, \dots, f_N\}$ is expressed as (19). In the following discussions, \mathbf{H}_s refers exclusively to the channel matrix associated with the sampled-frequency indices, while those without the subscript s correspond to the full-subband counterparts.

$$\begin{aligned} \hat{\mathbf{H}}_s &= [\mathbf{h}'(f_1), \mathbf{h}'(f_2), \dots, \mathbf{h}'(f_N)] \\ &= \hat{\mathbf{C}}_3 \left[(f_1 \mathbf{I} - \mathbf{A}_3)^{-1} \mathbf{B}_3 \dots (f_N \mathbf{I} - \mathbf{A}_3)^{-1} \mathbf{B}_3 \right] \end{aligned} \quad (19)$$

For notational compactness, define \mathbf{Y} as (20) where $r_f < 2N$.

$$\mathbf{Y} = \left[(f_1 \mathbf{I} - \mathbf{A}_3)^{-1} \mathbf{B}_3 \dots (f_N \mathbf{I} - \mathbf{A}_3)^{-1} \mathbf{B}_3 \right] \in \mathbb{C}^{r_f \times 2N} \quad (20)$$

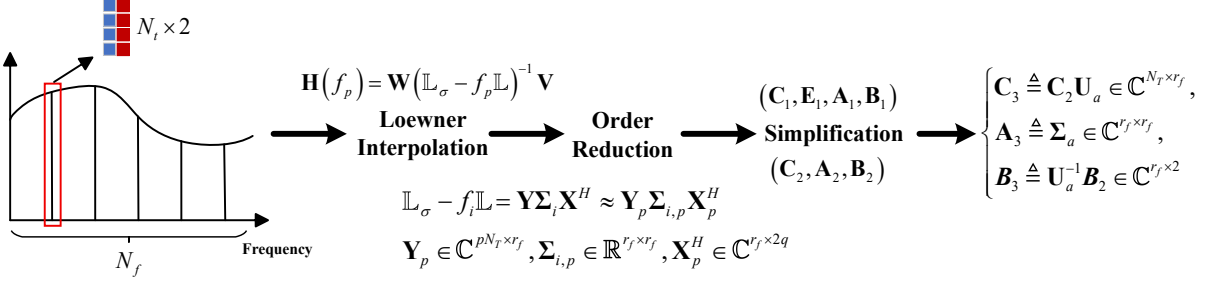


Fig. 2. The illustration of the LI-based CSI compression scheme.

Then, the squared \mathcal{F} -norm of the reconstructed error $\Delta \mathbf{H}_s$ can be written as:

$$\begin{aligned} \|\Delta \mathbf{H}_s\|_F^2 &= \|\mathbf{H}_s - (\mathbf{C}_3 + \Delta \mathbf{C}_3) \mathbf{Y}\|_F^2 \\ &= \|\Delta \mathbf{C}_3 \mathbf{Y}\|_F^2 = \text{tr} \left((\Delta \mathbf{C}_3 \mathbf{Y})^H (\Delta \mathbf{C}_3 \mathbf{Y}) \right) \\ &= \text{tr} \left(\mathbf{Y}^H \Delta \mathbf{C}_3^H \Delta \mathbf{C}_3 \mathbf{Y} \right) \\ &= \text{tr} \left(\Delta \mathbf{C}_3^H \Delta \mathbf{C}_3 \mathbf{Y} \mathbf{Y}^H \right) \end{aligned} \quad (21)$$

As shown in (21), the reconstruction error at the sampled points depends not only on $\Delta \mathbf{C}_3$ which is introduced by the compression in the spatial domain but is further amplified by $\mathbf{Y} \mathbf{Y}^H$. To eliminate this amplification effect, we aim to transform \mathbf{Y} into an orthogonal matrix such that $\mathbf{Y} \mathbf{Y}^H = \mathbf{I}$, thereby eliminating the error-scaling effect.

To achieve this, we perform the thin SVD to \mathbf{Y} as shown in (22).

$$\begin{aligned} \mathbf{Y} &= \mathbf{U}_Y \Sigma_Y \mathbf{V}_Y^H \\ \mathbf{U}_Y &\in \mathbb{C}^{r_f \times r_f}, \Sigma_Y \in \mathbb{R}^{r_f \times r_f}, \mathbf{V}_Y^H \in \mathbb{C}^{r_f \times 2N} \end{aligned} \quad (22)$$

We then replace \mathbf{Y} with \mathbf{V}_Y^H and absorb the remaining factors \mathbf{U}_Y and Σ_Y into \mathbf{C}_3 , yielding a transformed basis as:

$$\mathbf{C}_4 \triangleq \mathbf{C}_3 \mathbf{U}_Y \Sigma_Y \in \mathbb{C}^{N_t \times r_f} \quad (23)$$

The reconstruction error of this adjusted scheme is given in (24). Compared to (21), it is obvious that the error-amplification effect of $\mathbf{Y} \mathbf{Y}^H$ has been fully removed.

$$\begin{aligned} \|\Delta \mathbf{H}_s\|_F^2 &= \|\mathbf{H}_s - (\mathbf{C}_4 + \Delta \mathbf{C}_4) \mathbf{V}_Y^H\|_F^2 \\ &= \|\Delta \mathbf{C}_4 \mathbf{V}_Y^H\|_F^2 = \|\Delta \mathbf{C}_4\|_F^2 \end{aligned} \quad (24)$$

To facilitate the auto-encoder-based compression in the spatial domain, we further enhance the sparsity of \mathbf{C}_4 with DFT. Accordingly, the matrix fed into the auto-encoder becomes (25):

$$\mathbf{C}_5 = \mathbf{F}_a \mathbf{C}_4 \in \mathbb{C}^{N_t \times r_f} \quad (25)$$

where $\mathbf{F}_a \in \mathbb{C}^{N_t \times N_t}$ denotes the unitary DFT matrix with $(\mathbf{F}_a)_{i,j} = \frac{1}{\sqrt{N_t}} e^{-j2\pi(i-1)(j-1)/N_t}$. Since no truncation is performed on the sparse matrix \mathbf{C}_5 , the sparsity enhancement step does not introduce additional reconstruction errors as proved in (26).

$$\begin{aligned} \|\Delta \mathbf{C}_4\|_F^2 &= \|\dot{\mathbf{C}}_4 - \mathbf{C}_4\|_F^2 = \|\mathbf{F}_a^H \dot{\mathbf{C}}_5 - \mathbf{F}_a^H \mathbf{C}_5\|_F^2 \\ &= \|\mathbf{F}_a^H \Delta \mathbf{C}_5\|_F^2 = \|\Delta \mathbf{C}_5\|_F^2 \end{aligned} \quad (26)$$

Assuming that the BS has obtained the recovered $\hat{\mathbf{C}}_5$ from the decoder, the interpolation of $\hat{\mathbf{H}}(f_p)$ (defined in (15)) at any given frequency index f_p requires to reconstruct $\hat{\mathbf{C}}_3$ from $\hat{\mathbf{C}}_5$. This reconstruction corresponds the reverse process of (25) and (23) which is given by (27):

$$\hat{\mathbf{C}}_3 = \mathbf{F}_a^H \hat{\mathbf{C}}_5 \hat{\Sigma}_Y^{-1} \hat{\mathbf{U}}_Y^H \in \mathbb{C}^{N_t \times r_f} \quad (27)$$

$\hat{\mathbf{U}}_Y$ and $\hat{\Sigma}_Y$ are obtained from the SVD of $\hat{\mathbf{Y}}$ with the feedback $\{\hat{\mathbf{A}}_3, \hat{\mathbf{B}}_3\}$ and the sample index $\{f_1, f_2, \dots, f_N\}$ as defined in (20). In practice, uniform sampling is adopted for the LI in the frequency domain. Consequently, the BS and the UE only need to maintain a consistent sampling interval, and there is no need to explicitly feed back the indices of the sampled frequency points.

C. Implementation of the Rateless Auto-Encoder

The LI-MORNet that achieves the flexible compression with variable-length codewords is implemented through two steps as shown in Fig. 3. First, we introduce the fixed CR module based on a CNN-based auto-encoder architecture. In the feature extraction module of the encoder, we adopt a cascaded convolutional architecture that starts with several large-sized kernels and gradually transitions to smaller kernels. The number of channels gradually increases with the number of convolutional layers and then decreases. The strides of all feature extraction layers are $(1, 1)$, ensuring that the dimension of \mathbf{C}_5 remains unchanged while the network focuses on learning its feature representation. The activation functions are leaky rectified linear unit (Leaky ReLU) for all the convolutional layers. A fully connected (FC) layer is employed after the feature extraction to generate an initial compressed codeword whose length is $M \times 1$ (fixed CR). In the decoder, following the decompression layer, three residual blocks are used to further refine the reconstructed $\hat{\mathbf{C}}_5$.

Then, we introduce the flexible compression mechanism, which is applied after the feature compression module using a set of random binary masks. During the training phase, a set of masks as:

$$\{\mathbf{e}_{l_1}, \mathbf{e}_{l_2}, \dots, \mathbf{e}_{l_n}\}, \mathbf{e}_{l_i} \triangleq \left[\underbrace{1, 1, \dots, 1}_{l_i}, 0, 0, \dots, 0 \right]^T \in \mathbb{R}^{M \times 1}$$

is applied to the initial codeword \mathbf{v} to generate multiple virtually truncated vectors:

$$\{\mathbf{v}_1, \mathbf{v}_2, \dots, \mathbf{v}_n\}, \mathbf{v}_i = \mathbf{v} \odot \mathbf{e}_{l_i} \in \mathbb{R}^{M \times 1} \quad (28)$$

To ensure diversity in the truncation degrees, the length l_i of each mask is randomly sampled within a predefined interval as $l_i \sim \mathcal{U}(L_i^{\min}, L_i^{\max})$. Furthermore, the n intervals $\{[L_1^{\min}, L_1^{\max}], [L_2^{\min}, L_2^{\max}], \dots, [L_n^{\min}, L_n^{\max}]\}$ are designed to be mutually non-overlapping and equal in length, i.e. $L_i^{\max} - L_i^{\min} = \Delta L, \forall i \in \{1, 2, \dots, n\}$. Each masked codewords \mathbf{v}_i is then fed into the decoder to obtain a set of reconstructed matrices:

$$\{\hat{\mathbf{C}}_{5,1}, \hat{\mathbf{C}}_{5,2}, \dots, \hat{\mathbf{C}}_{5,n}\}, \hat{\mathbf{C}}_{5,i} = f_{de}(\mathbf{v}_i, \varphi_{de}) \quad (29)$$

For each reconstruction, we compute the corresponding mean square error (MSE) which is defines as:

$$\mathcal{L}_i(\theta_{en}, \varphi_{de}; l_i) = \left\| \mathbf{C}_5 - \hat{\mathbf{C}}_{5,i} \right\|_F^2 \quad (30)$$

We then take the weighted average of these MSE as the loss function as :

$$\mathcal{L}(\theta_{en}, \varphi_{de}) = \sum_{i=1}^n w_i \mathcal{L}_i(\theta_{en}, \varphi_{de}; l_i) \quad (31)$$

Since the magnitudes of individual MSE losses $\mathcal{L}_i(\theta_{en}, \varphi_{de}; l_i)$ may vary significantly across different tasks or output levels l_i , directly summing them could cause certain terms to dominate the overall optimization process. Consequently, the weights w_i are chosen to adjust the individual loss terms so that they contribute at comparable levels. The proposed LI-MORNet is trained using the adaptive moment estimation (Adam) optimizer and a cosine annealing schedule for the learning rate. With this training strategy, the compressed codeword are automatically ordered by importance: the elements appearing earlier in the codeword carry more critical feature information and thus receive higher priority during feedback transmission. As a result, the receiver does not need to obtain the entire codeword before initiating the decoding process. During the test stage, after the encoder outputs the codeword, the UE sequentially feeds back codewords of arbitrary length. Upon receiving the codewords, the BS pads them to length M before sending them to the decoder for reconstruction. Consequently, the BS can progressively reconstruct $\hat{\mathbf{C}}_5$ using only the first portion of the received codeword. This property makes the proposed framework particularly suitable for scenarios involving reception interruption or delayed decoding, which can be modeled as a channel with tail erasures. The detail procedure of the LI-MORNet is given in Algorithm 1.

V. VARIABLE-LENGTH WIDEBAND CSI FEEDBACK WITH ROBUST QUANTIZATION

In this section, we develop a robust quantization scheme for the proposed CSI compression framework. We first summarize the overall codewords for feedback and design dedicated quantization schemes respectively based on their impact on the reconstruction. We then outline the complete procedure that integrates the quantization scheme into the end-to-end reconstruction pipeline.

Algorithm 1 The proposed LI-MORNet

Input: Training set: \mathcal{D}_{train} ; Testing set: \mathcal{D}_{test} ; Initial codeword length: M ; Random mask interval: $\{[L_1^{\min}, L_1^{\max}], [L_2^{\min}, L_2^{\max}], \dots, [L_n^{\min}, L_n^{\max}]\}$; Maximum epoches: E ; Test feedback length l_t , ($L_1^{\min} \leq l_t \leq L_n^{\max}$);

- 1: **[Off-line training stage]:**
- 2: **Initialization:** $\theta_{en}^0, \varphi_{de}^0$.
- 3: **for** $i = 1 \dots E$ **do**
- 4: **for** \mathbf{C}_5 in \mathcal{D}_{train} **do**
- 5: **for** $m = 1 \dots n$ **do**
- 6: Obtain codeword \mathbf{v} from the encoder;
- 7: Randomly sampled mask length from the m -th interval $l_m \sim \mathcal{U}(L_m^{\min}, L_m^{\max})$
- 8: Apply mask \mathbf{e}_{l_m} to \mathbf{v} and obtain virtually truncated vector \mathbf{v}_m ;
- 9: Feed \mathbf{v}_m to the decoder and obtain reconstructed $\hat{\mathbf{C}}_{5,m}$;
- 10: Compute the MSE according to (30);
- 11: **end for**
- 12: Update $\theta_{en}^i, \varphi_{de}^i$ via end-to-end training with the loss defined in (31);
- 13: **end for**
- 14: **end for**
- 15: **Output:** $\theta_{en}^E, \varphi_{de}^E$.
- 16: **[Online testing stage]:**
- 17: **for** \mathbf{C}_5 in \mathcal{D}_{test} **do**
- 18: Obtain codeword \mathbf{v} from the encoder;
- 19: Apply mask \mathbf{e}_{l_t} to the codeword \mathbf{v} and obtain \mathbf{v}_t ;
- 20: Feed \mathbf{v}_t to the decoder and obtain $\hat{\mathbf{C}}_{5,t}$;
- 21: **end for**
- 22: **Output:** $\hat{\mathbf{C}}_{5,t}$.

A. Robust Quantization Algorithm

By combining the LI-based compression in the frequency domain (Section III) with the rateless auto-encoder-based compression in the spatial domain (Section IV), the resulting feedback codeword set consists of:

$$\mathbf{z} = \{\mathbf{A}_3 \in \mathbb{C}^{r_f \times r_f}, \mathbf{B}_3 \in \mathbb{C}^{r_f \times 2}, \mathbf{v}_{l_m} \in \mathbb{R}^{l_m}\}. \quad (32)$$

For the quantization of the complex-valued matrices \mathbf{A}_3 and \mathbf{B}_3 , according to the transformation strategy designed to suppress the error amplification in Section IV-B, \mathbf{V}_Y must retain unitary. As defined in (20), \mathbf{Y} is constructed from $\mathbf{A}_3, \mathbf{B}_3$ and the set of sampled frequency indices $\{f_1, f_2, \dots, f_N\}$. Therefore, $\mathbf{A}_3, \mathbf{B}_3$ need to be quantized with sufficiently high precision to ensure that the reconstruction $\hat{\mathbf{V}}_Y$ satisfies $\hat{\mathbf{V}}_Y^H \hat{\mathbf{V}}_Y \approx \mathbf{I}_{r_f}$. As a result, we perform uniform quantization to both the magnitude and phase components of \mathbf{A}_3 and \mathbf{B}_3 with high quantization bits. Considering their distinct numerical characteristics, tailored preprocessing is introduced to improve the quantization efficiency. Specifically, the distribution of the elements in \mathbf{A}_3 and \mathbf{B}_3 in the constellation diagram forms a uniform ring pattern. This suggests that, after appropriate scaling and bias adjustment, both the phase and amplitude of the two matrices exhibit a uniform distribution.

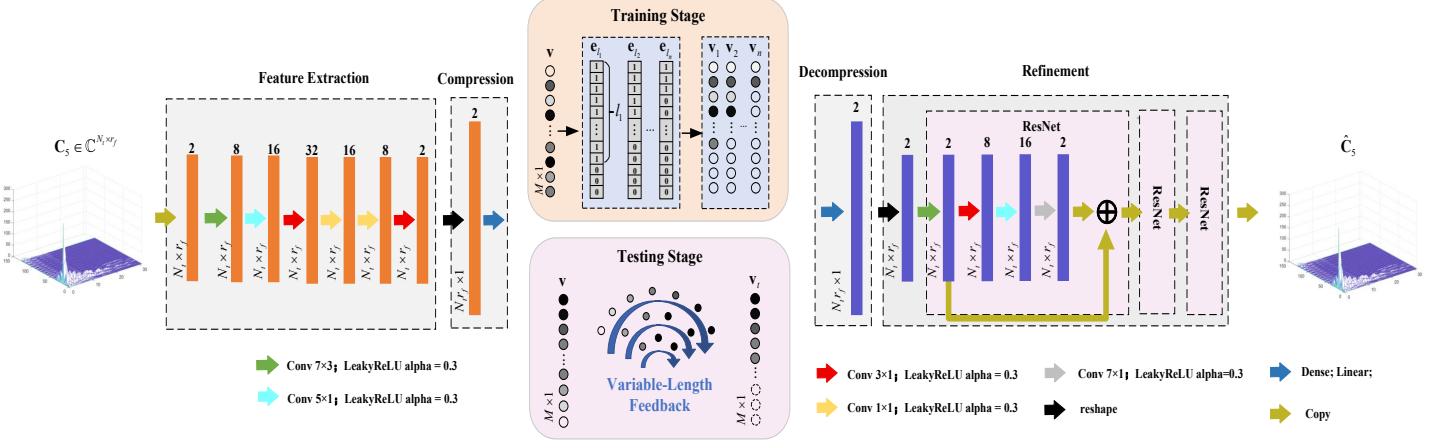


Fig. 3. The illustration of the proposed LI-MORnet.

Since the center of $\text{diag}(\mathbf{A}_3)$ element distribution is offset from the origin, a bias adjustment is necessary. On the other hand, while the center of \mathbf{B}_3 element distribution is at the origin, its amplitude range is relatively large, requiring scaling before the quantization to ensure an optimal representation. Consequently, for the diagonal matrix \mathbf{A}_3 , we subtract a bias before performing uniform quantization to its diagonal elements. For \mathbf{B}_3 , a scaling factor is applied before the quantization to accommodate its broader value distribution. For the real-valued vector \mathbf{v}_{l_m} , two quantization schemes are employed: Uniform quantization and μ -law quantization.

Though the quantization bits of \mathbf{v}_{l_m} basically determines the overall feedback overhead, we find that the reconstruction error exhibits greater sensitivity to $\Delta \mathbf{V}_Y$ which is solely determined by the quantization error of \mathbf{A}_3 and \mathbf{B}_3 . Specifically, (24) can be further expressed as (33) when considering the quantization error of all the feedback codewords. The Hessian matrices of the objective function $f = \|\Delta \mathbf{H}_s\|_F^2$ with respect to $\Delta \mathbf{C}_4$ and $\Delta \mathbf{V}_Y$ are given in (34) and (35), where $\hat{\mathbf{V}}_Y$ and $\hat{\mathbf{C}}_4$ denote the reconstruction matrices perturbed by the quantization of codewords. Numerical results confirm that $\|\mathcal{H}_{\Delta \mathbf{V}_Y} f\|_F^2 > \|\mathcal{H}_{\Delta \mathbf{C}_4} f\|_F^2$ indicating that the reconstruction error $\|\Delta \mathbf{H}_s\|_F^2$ is more sensitive to variations in $\Delta \mathbf{V}_Y$. This suggests that greater attention should be devoted to the quantization bit allocation for \mathbf{A}_3 and \mathbf{B}_3 .

$$\|\Delta \mathbf{H}_s\|_F^2 = \left\| \mathbf{H}_s - (\mathbf{C}_4 + \Delta \mathbf{C}_4)(\mathbf{V}_Y + \Delta \mathbf{V}_Y)^H \right\|_F^2 \quad (33)$$

$$\begin{aligned} \mathcal{H}_{\Delta \mathbf{C}_4} f &= \begin{bmatrix} (\hat{\mathbf{V}}_Y^H \hat{\mathbf{V}}_Y)^* \otimes \mathbf{I}_{N_t} & \mathbf{0} \\ \mathbf{0} & (\hat{\mathbf{V}}_Y^H \hat{\mathbf{V}}_Y) \otimes \mathbf{I}_{N_t} \end{bmatrix} \\ &\approx \begin{bmatrix} \mathbf{I}_{r_f N_t} & \mathbf{0} \\ \mathbf{0} & \mathbf{I}_{r_f N_t} \end{bmatrix} \end{aligned} \quad (34)$$

$$\mathcal{H}_{\Delta \mathbf{V}_Y} f = \begin{bmatrix} (\hat{\mathbf{C}}_4^H \hat{\mathbf{C}}_4)^* \otimes \mathbf{I}_{2N} & \mathbf{0} \\ \mathbf{0} & (\hat{\mathbf{C}}_4^H \hat{\mathbf{C}}_4) \otimes \mathbf{I}_{2N} \end{bmatrix} \quad (35)$$

Guided by this insight, we fine-tune the quantization bits of \mathbf{A}_3 and \mathbf{B}_3 . Specifically, the UE detects potentially abnormal

reconstruction samples in advance before feedback by evaluating the \mathcal{F} -norm of the gradient matrix. After discarding the second-order terms, the gradient matrix of $\|\Delta \mathbf{H}_s\|_F^2$ can be expressed as (36).

$$\begin{aligned} \mathbf{G} &= \frac{\partial \|\Delta \mathbf{H}_s\|_F^2}{\partial \Delta \mathbf{V}_Y} = (\mathbf{C}_4^H \mathbf{C}_4 \Delta \mathbf{V}_Y^H + \Delta \mathbf{C}_4^H \mathbf{C}_4 \Delta \mathbf{V}_Y^H \\ &\quad (\mathbf{C}_4 + \Delta \mathbf{C}_4)^H \Delta \mathbf{C}_4 (\mathbf{V}_Y + \Delta \mathbf{V}_Y)^H)^T \\ &\approx (\mathbf{C}_4^H \mathbf{C}_4 \Delta \mathbf{V}_Y^H + \mathbf{C}_4^H \Delta \mathbf{C}_4 \mathbf{V}_Y^H)^T \end{aligned} \quad (36)$$

Further, \mathbf{G} can be written as $\mathbf{G} = \mathbf{G}_1 + \mathbf{G}_2$ where:

$$\mathbf{G}_1 = (\mathbf{C}_4^H \mathbf{C}_4 \Delta \mathbf{V}_Y^H)^T \quad (37)$$

$$\mathbf{G}_2 = (\mathbf{C}_4^H \Delta \mathbf{C}_4 \mathbf{V}_Y^H)^T \quad (38)$$

Consequently, we can derive the upper bound for the \mathcal{F} -norm of \mathbf{G} :

$$\|\mathbf{G}\|_F \leq \|\mathbf{G}_1\|_F + \|\mathbf{G}_2\|_F \quad (39)$$

Since $\|\mathbf{G}_2\|_F$ is independent of $\Delta \mathbf{V}_Y$, by focusing on $\|\mathbf{G}_1\|_F$ we can simplify the overall analysis and derive a useful insight into how the CSI reconstruction error $\|\Delta \mathbf{H}_s\|_F^2$ behaves as a function of the quantization errors of the other two matrices \mathbf{A}_3 and \mathbf{B}_3 . Specifically, when $\|\mathbf{G}_1\|_F$ has large values, it indicates that the quantization system is far from the optimal state and the reconstruction error is likely to be large. Note that $\|\mathbf{G}_1\|_F$ is fully known at the UE side, consequently providing an efficient way to anticipate the potential recovery anomalies prior to feedback. The proposed algorithm, as summarized in Algorithm 2, can perform quantization adjustments on the CSI samples likely to exhibit significant reconstruction errors, thereby enhancing the overall robustness of the feedback scheme.

B. Summary of the Overall Framework

The overall workflow of the proposed wideband CSI feedback scheme, which integrates the LI framework, DL-based spatial compression and the robust quantization module, is illustrated in Fig. 4.

Algorithm 2 The proposed Robust Quantization Algorithm for \mathbf{A}_3 and \mathbf{B}_3 .

Input: LI-MOR basis matrices: $\{\mathbf{C}_4, \mathbf{A}_3, \mathbf{B}_3\}$; Sampled frequency indices: $\{f_1, f_2, \dots, f_N\}$; Error threshold: ϵ ;

Initialize: Quantization bits (amplitude/phase) for $\{\mathbf{A}_3, \mathbf{B}_3\}$: (A, P) ; Adjustment step size for quantization bits: $(\Delta A, \Delta P)$;

Step1: Obtain \mathbf{Y} as (20) with $\{\mathbf{A}_3, \mathbf{B}_3\}$ and $\{f_1, f_2, \dots, f_N\}$; Perform thin SVD to \mathbf{Y} and obtain \mathbf{V}_Y following (22);

Step2: Perform uniform quantization to $\{\mathbf{A}_3, \mathbf{B}_3\}$ with (A, P) bits and reconstruct $\{\hat{\mathbf{A}}_3, \hat{\mathbf{B}}_3\}$; Compute $\hat{\mathbf{V}}_Y$ with $\{\hat{\mathbf{A}}_3, \hat{\mathbf{B}}_3\}$ as (20) and (22); Obtain the error matrix $\Delta \mathbf{V}_Y = \hat{\mathbf{V}}_Y - \mathbf{V}_Y$; Obtain \mathbf{G}_1 as (37);

Step3: If $\|\mathbf{G}_1\|_F \geq \epsilon$, $A = A + \Delta A$, $P = P + \Delta P$ and go to **Step 2**;

Step4: If $\|\mathbf{G}_1\|_F < \epsilon$, terminate the algorithm;

Output: Binary codes of quantized $\{\mathbf{A}_3, \mathbf{B}_3\}$ with (A, P) : $\mathbf{b}_A, \mathbf{b}_B$;

At the UE side, the original channel slice $\mathbf{H} = \mathcal{H}_{i,:,:} \in \mathbb{C}^{2N_t \times N_f}$ corresponding to the i -th receive antenna is initially compressed in the frequency domain via LI-MOR (the blue block in Fig. 4 as introduced in Section III). This process constructs the LI bases $\{\mathbf{C}_3, \mathbf{B}_3, \mathbf{A}_3\}$. Among them, \mathbf{B}_3 and \mathbf{A}_3 exhibit simple structures, whereas $\mathbf{C}_3 \in \mathbb{C}^{N_t \times r_f}$ still retains redundant information in the spatial domain, especially when N_t is large for massive MIMO systems. Subsequently, \mathbf{C}_3 undergoes preprocessing through unitary matrix merging and sparsity enhancement to control the cascaded errors before being fed into the rateless auto-encoder (the orange block in Fig. 4 as introduced in Section IV). After the compression in both the frequency and spatial domains, the resulting codewords are given by $\mathbf{z}_i = \{\mathbf{v}_t, \mathbf{A}_3, \mathbf{B}_3\}$, to which different quantization strategies are applied to ensure the robustness of the overall scheme across different channel samples (the gray block in Fig. 4 as introduced in Subsection V-A).

At the BS side, the received binary bits are first dequantized according to the corresponding quantization scheme, yielding $\hat{\mathbf{z}}_i = \{\hat{\mathbf{v}}_t, \hat{\mathbf{A}}_3, \hat{\mathbf{B}}_3\}$. The codeword $\hat{\mathbf{v}}_t$ is fed into the decoder to reconstruct $\hat{\mathbf{C}}_5$. By applying the reverse preprocessing described as (27), the BS further reconstructs $\hat{\mathbf{C}}_3$. With $\{\hat{\mathbf{C}}_3, \hat{\mathbf{A}}_3, \hat{\mathbf{B}}_3\}$, the BS can recover $\hat{\mathbf{H}}$ via the interpolation function defined in (15). It is worth noting that the proposed variable-length feedback operates at the codeword level. Therefore, the UE needs to append several additional bits to indicate the quantization bit width of each codeword (the overhead of these indicator bits is negligible), enabling proper dequantization at the BS.

VI. SIMULATION RESULTS

In this section, we evaluate the performance of the proposed wideband CSI feedback scheme. First, we describe the parameter settings of the wideband channels and the dataset. Then, we present the simulation results including the feedback precision and overhead, the computational complexity, the

parameter storage and the spectral efficiency of the proposed algorithm and the baseline schemes.

A. Parameter Setting and Channel Data

We consider the wideband CDL-A and CDL-B channels in 3GPP 38.901 [27]. To facilitate the simulation comparison, we separate the 400M wideband channel matrix and take one of the 100M bandwidth as an example. The main parameters are listed in Table I. Note that the size of the feedback channel slice for the proposed scheme is $\mathcal{H}_{i,:,:} \in \mathbb{C}^{256 \times 3300}$. When generating the channel dataset, different random seeds (1~1000000) are used to ensure that the resulting channel samples are non-overlapping. The dataset is partitioned into 50,000 samples for training, 10,000 for validation, and 10,000 for testing.

TABLE I
MAIN CHANNEL PARAMETERS

Channel profile	CDL-A/CDL-B (NLOS)
Carrier center frequency f_c	6.9 GHz
Transmitting antenna N_t	16×8 (UPA)
Receiving antenna N_r	2
Antenna polarization	$\pm 45^\circ$
RMS Delay spread	30 ns
Number of resource blocks N_{RB}	275
Subcarrier spacing	30 kHz
Number of Subcarriers N_f	$12 \times 275 = 3300$
Bandwidth	100 MHz
Number of layer R	2

B. NMSE and Feedback Overhead Performance

The normalized MSE (NMSE) is used to evaluate the recovery accuracy of CSI matrix $\mathbf{H} = \mathcal{H}_{i,:,:} \in \mathbb{C}^{256 \times 3300}$, as defined in (40). Our overall principle is to make a fair comparison by showing that the proposed scheme can achieve a smaller reconstruction error with equal or less feedback overhead which is either the complex numbers (when evaluating the performance without quantization) or the number of the binary bits (when evaluating the performance with quantization).

$$NMSE = E \left\{ \left\| \hat{\mathbf{H}} - \mathbf{H} \right\|_F^2 / \left\| \mathbf{H} \right\|_F^2 \right\} \quad (40)$$

We compare the proposed LI-MORNet to the following baseline schemes.

- **SM-CsiNet+** [17]: The encoder achieves multi-rate feedback through multiple cascaded FC layers. The BS must deploy multiple decoders corresponding to the CRs. To extend the set of compression-rate nodes, the encoder architecture must be modified, additional decoders must be deployed at the BS, and the entire model must be retrained.
- **PM-CsiNet+** [17]: The feature extraction module is the same as that of SM-CsiNet+. But the encoder achieves multi-rate feedback through parallel FC layers which is a more compact model. The BS still needs multiple decoders.
- **CL-Net** [14]: A high-precision CSI feedback network that effectively integrates the real and imaginary parts

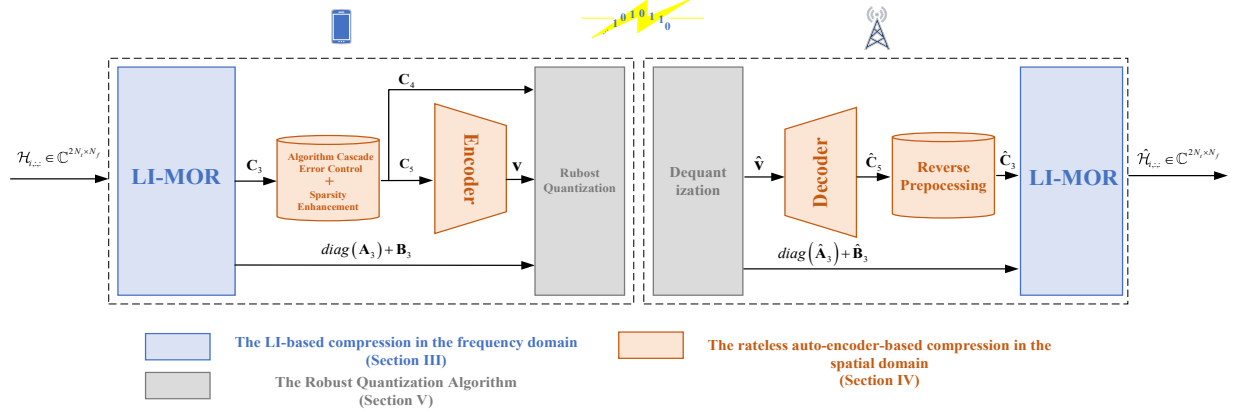


Fig. 4. The workflow of the overall framework.

and utilizes spatial attention mechanism. However, each pre-trained model supports feedback at only one CR. Changing the CR requires retraining the model and deploying additional encoder-decoder pairs at both the UE and the BS.

All the baseline schemes employ the DFT for channel characterization as the preprocessing, which involves reconstructing the sparse angular-delay domain channel representation $\tilde{\mathbf{H}} = \mathbf{F}_d \mathbf{H} \mathbf{F}_a^H$. Following the truncation ratio adopted in prior work [12], the number of retained columns in the delay domain is set to $N_c = 103$. Truncation is applied only in the delay domain because it has substantially higher dimension and exhibits stronger sparsity compared with the angular domain. All networks were trained for 1,000 epochs, using a cosine annealing schedule for the learning rate. For the proposed LI-MORNet, the initial codeword length M is set to N_{trf} so that the initial CR_s is $1/2$ and the interval length of the random mask is set to $\Delta L = 255$ with $n = 7$, $L_1^{min} = 256$, $L_7^{max} = 2048$ and $L_i^{max} + 1 = L_{i+1}^{min}$, $\forall i = 1, \dots, n-1$ so that the supported range of the CR by the rateless auto-encoder is $\frac{1}{32} \leq CR_s \leq \frac{1}{4}$. The weight coefficients in (31) is set to $\{w_1, w_2, w_3, w_4, w_5, w_6, w_7\} = \{25, 20, 10, 5, 1, 1, 1\}$. The training curve of LI-MORNet is shown in Fig. 5.

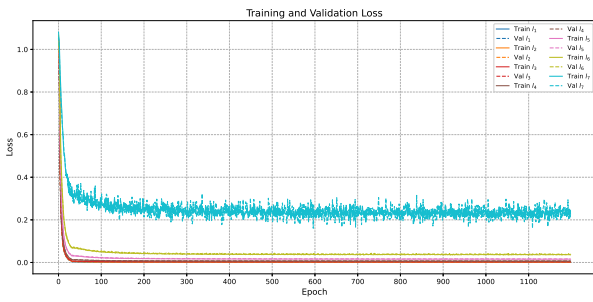


Fig. 5. The Training Curve of the LI-MORNet.

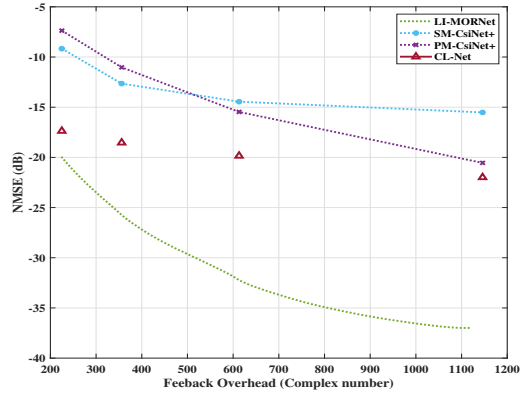
1) *Performance without Quantization*: Fig. 6 illustrates the performance comparison of different CSI feedback schemes without quantization. For the two multi-rate feedback algorithms, the pre-trained model supports only the CRs corresponding to the nodes on the curve. For the single-rate

feedback algorithm, each node represents an individual model pre-trained for a specific CR. In contrast, our proposed LI-MORNet enables a single model to support feedback at any point along the curve. Based on the simulation results, our proposed model achieves much higher reconstruction precision than all multi-rate feedback schemes, and it even outperforms the single-rate network (CL-Net) for most cases. It only exhibits lower reconstruction accuracy than the single-rate network CL-Net under low feedback overhead for the CDL-B channel. However, even for this case, it still offers clear advantages in smaller parameter storage and computational complexity and the flexibility of the trade-off between feedback overhead and reconstruction accuracy, as will be further analyzed in Subsection VI-C.

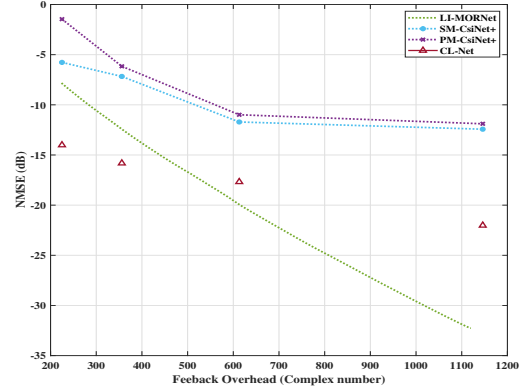
The number of feedback complex numbers of our proposed LI-MORNet is $d = (N_t \times r_f \times CR_s + r_f \times 3)$ where CR_s is defined as (17). We make an initial selection of r_f according to the number of paths in the delay domain and then fine-tune it according to the numerical simulation results. With $r_f = 32$ and $\frac{1}{32} \leq CR_s \leq \frac{1}{4}$, the overall CR which is defined as $CR = d/2N_t N_{sc}$ that we compare falls in the range $\frac{1}{3770} \leq CR \leq \frac{1}{800}$.

2) *Impact of the Robust Quantization Algorithm*: Fig. 7 illustrates the effectiveness of the proposed robust quantization scheme under CDL-A and CDL-B channel models. The horizontal axis denotes the channel sample index. For clarity of presentation, 1000 random samples are selected from the test set and shown in the figure. Note that to distinguish between the curves, we added different offsets when plotting the graph.

As introduced in Subsection V-A, the yellow curve represents $\|\mathbf{G}\|_F$, which quantifies the sensitivity of the quantization error of $\mathbf{A}_3, \mathbf{B}_3$ with respect to the perturbation at the sampling point. The purple curve denotes $\|\mathbf{G}_1\|_F$, a constant known at the UE that serves as an indicator for identifying samples potentially prone to unstable or anomalous recovery. It can be observed from the results that both the purple and yellow curves remain relatively small for the majority of channel samples. However, at several sample indices, the curves exhibit pronounced peaks. These peaks indicate that the system is momentarily far from its optimal point, leading to a larger reconstruction error at the BS. This sensitivity behavior is directly confirmed by the blue curve, which plots the



(a) CDL-A



(b) CDL-B

Fig. 6. The NMSE performance without quantization of different CSI feedback schemes.

NMSE using the conventional quantization strategy (without the robust quantization scheme). The peaks nearly coincide with those of the yellow detection curve which means that with the known $\|\mathbf{G}_1\|_F$ at the UE side the potential low-accuracy recovery samples can be accurately detected. The orange curve further demonstrates that, with the proposed robust quantization scheme, these anomalous samples can be reconstructed with high precision, and the recovery at the BS remains stable across the entire sample set.

3) *Performance with Quantization*: Fig. 8 shows the performance comparison of different CSI feedback schemes with quantization. For all baseline algorithms, we applied both uniform quantization and μ -law quantization using codeword lengths of $4 \sim 7$ bits. We then select the optimal configuration by jointly considering the compression ratio, quantization scheme (i.e., number of bits and quantization method), and feedback accuracy. Specifically, among the configurations with comparable feedback overhead, we chose the one that achieves the highest feedback accuracy.

C. Computational Complexity Comparison

We use the number of floating point operations (FLOPs) to evaluate the NN complexity. The total computational com-

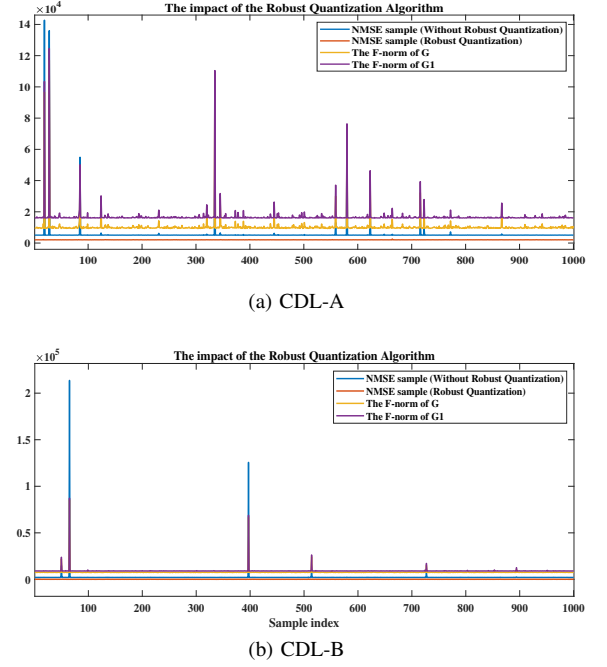


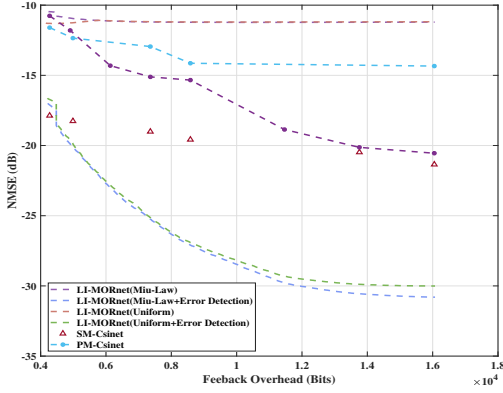
Fig. 7. The impact of the Robust Quantization Algorithm.

plexity of the proposed LI-MORNet consists of two major components.

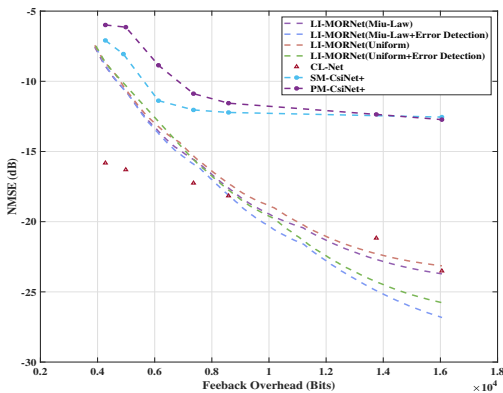
For the LI-based compression at the UE, only the dominant term is considered in the final result, as expressed in (10). For the SVD of a $m \times n$ matrix, retaining the leading k singular components via rank-revealing QR factorization requires $\mathcal{O}(mnk)$ FLOPs [11][12]. Consequently, the computational complexity of the compression in the frequency domain at the UE is $\mathcal{O}(2qpN_{Trf})$. At the BS side, the dominant computational complexity at the BS arises from the interpolation over the full set of subcarriers as shown in (15). Since \mathbf{A}_3 is a diagonal matrix and $\mathbf{B}_3 \in \mathbb{C}^{r_f \times 2}$, we calculate $\widehat{\mathbf{H}}(f_p) = \widehat{\mathbf{C}}_3 \left(f_p \mathbf{I} - \widehat{\mathbf{A}}_3 \right)^{-1} \widehat{\mathbf{B}}_3 \in \mathbb{C}^{N_T \times 2}$ for all N_{sc} subcarriers, yielding a total computational complexity of $\mathcal{O}(2N_T N_{sc} r_f)$. Therefore, the overall algorithmic complexity of the LI-based compression and decompression is $\mathcal{O}(2qpN_{Trf}) + \mathcal{O}(2N_T N_{sc} r_f)$. The typical values of p and q are 137 and 138 respectively.

For the compression and the decompression in the spatial domain, the FLOPs of the rateless auto-encoder are 91.767M. We combine the computational complexity in both the frequency and the spatial domains for our proposed scheme to ensure a fair comparison with the baselines. For the single-rate baseline network, we include the parameter storage and FLOPs of all supported CR branches.

Table II presents the comparison of the computational complexity and parameter storage of different CSI feedback schemes. Compared to the baseline networks, our proposed scheme achieves reductions in both parameter storage and total computational complexity. In fact, our scheme offers lower neural-network complexity, while the LI-based compression in the frequency domain introduces additional computational complexity, yet enables higher reconstruction accuracy and



(a) CDL-A



(b) CDL-B

Fig. 8. The NMSE performance with quantization of different CSI feedback schemes.

reduced parameter storage.

TABLE II
COMPLEXITY AND STORAGE COMPARISON

Scheme	LI-MORNet	CL-Net	SM-CsiNet+	PM-CsiNet+
FLOPs	428.05M	498.2M	788.1M	786.4M
Storage	67.1M	123.5M	93.1M	91.3M

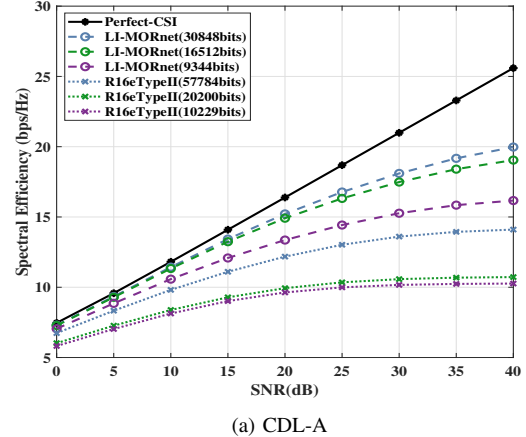
D. Spectral Efficiency Comparison

In this section, we adopt the R16 eType-II codebook (mode 2,4,6) as the baseline for spectral-efficiency comparison because eType-II and our proposed scheme feed back different types of CSI respectively (precoder-related information \mathbf{W} versus the full channel matrix \mathcal{H}). As a result, directly comparing their NMSE would be neither fair nor physically meaningful. Instead, we evaluate both schemes under the same downlink precoding framework and compare their achievable spectral efficiency, thereby providing a consistent and meaningful assessment of end-to-end system performance. The simulation results are illustrated in Fig. 9. In the considered setup, the UE first obtains a perfectly estimated downlink channel $\mathcal{H} = [\mathbf{H}_1, \mathbf{H}_2, \dots, \mathbf{H}_{N_f}] \in \mathbb{C}^{N_r \times 2N_t \times N_f}$ and derives the receive combining vectors from its singular value

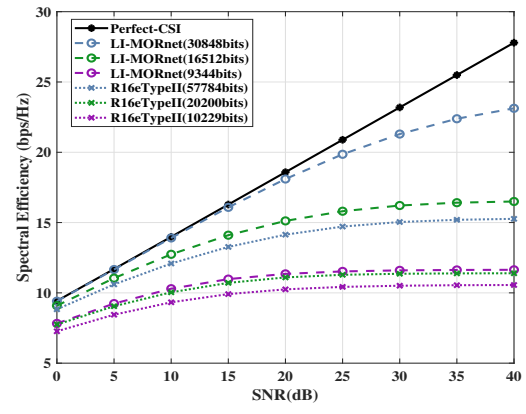
decomposition (SVD). Meanwhile, the BS reconstructs the channel information based on the feedback and applies the corresponding SVD-based precoding to facilitate downlink transmission as described in Section II. Based on this configuration, the achievable spectral efficiency can be expressed as $\frac{1}{N_f} \sum_{f=1}^{N_f} \sum_{l=1}^{N_t} \Gamma_{l,f}$ where

$$\Gamma_{l,f} = \log \left(1 + \frac{\left| \mathbf{u}_{l,f}^H \mathbf{H}_f \hat{\mathbf{v}}_{l,f} \right|^2}{\sum_{j=1, j \neq l}^R \left| \mathbf{u}_{j,f}^H \mathbf{H}_f \hat{\mathbf{v}}_{j,f} \right|^2 + \frac{P_n}{P_t} \left\| \mathbf{u}_{l,f} \right\|^2} \right)$$

$\mathbf{H}_f \in \mathbb{C}^{N_r \times 2N_t}$ represents the channel matrix at the f -th subband. $\mathbf{u}_{l,f}$ denotes the combining vector for stream l of subband f , obtained using the perfectly estimated channel matrix $\mathbf{H}_f = \mathbf{U}_f \Sigma_f \mathbf{V}_f^H$. Specifically, the l -th column of \mathbf{U}_f , denoted as $\mathbf{u}_{l,f}$, is adopted as the receive combiner at the UE. While the right singular vector $\hat{\mathbf{v}}_{l,f}$ of the reconstructed channel matrix $\hat{\mathbf{H}}_f = \hat{\mathbf{U}}_f \hat{\Sigma}_f \hat{\mathbf{V}}_f^H$ (the l -th column of $\hat{\mathbf{V}}_f$) is used as the corresponding transmit precoder at the BS. This setup reflects a practical FDD feedback scenario, where the UE utilizes the perfectly estimated channel to compute the receive combining vectors, while the BS reconstructs the CSI from feedback and applies the corresponding SVD-based precoding for downlink transmission.



(a) CDL-A



(b) CDL-B

Fig. 9. The performance of the spectral efficiency.

VII. CONCLUSION

We propose a variable-length wideband CSI feedback scheme based on LI and DL, enabling high-precision CSI reconstruction while offering a flexible trade-off between feedback overhead and reconstruction accuracy within the quantization framework. In the frequency domain, we develop an LI-based CSI interpolation model that constructs a set of initial bases, ensuring perfect CSI recovery at sampled subcarriers and high-precision fitting across the remaining frequency indices. With the MOR in the LI framework and the further simplification, two of the bases become structurally sparse and lightweight. This allows us to focus on compressing the dominant basis, which still contains spatial redundancy and has the dimension determined by the number of antennas. We design a cascaded spatial compression scheme that employs matrix transformations to prevent the cascaded error amplification and enhance sparsity. Variable-length codeword feedback is then enabled through a rateless auto-encoder. In addition, we develop dedicated quantization strategies for the codewords derived from both the frequency-domain and spatial-domain compression, improving the robustness of the overall system across different channel samples. The simulation results demonstrate that our scheme significantly outperforms the baseline schemes in both CSI recovery accuracy and the communication system performance on wideband channels.

REFERENCES

- [1] Fredrik Rusek, Daniel Persson, Buon Kiong Lau, Erik G. Larsson, Thomas L. Marzetta, Ove Edfors, and Fredrik Tufvesson. Scaling up mimo: Opportunities and challenges with very large arrays. *IEEE Signal Processing Magazine*, 30(1):40–60, 2013.
- [2] Qi Zhang, Zhaohua Lu, Shi Jin, Kai-Kit Wong, Hongbo Zhu, and Michail Matthaiou. Power scaling of massive mimo systems with arbitrary-rank channel means and imperfect csi. In *2013 IEEE Global Communications Conference (GLOBECOM)*, pages 4157–4162, 2013.
- [3] Hongxiang Xie, Feifei Gao, and Shi Jin. An overview of low-rank channel estimation for massive mimo systems. *IEEE Access*, 4:7313–7321, 2016.
- [4] David J. Love, Robert W. Heath, Vincent K. N. Lau, David Gesbert, Bhaskar D. Rao, and Matthew Andrews. An overview of limited feedback in wireless communication systems. *IEEE Journal on Selected Areas in Communications*, 26(8):1341–1365, 2008.
- [5] Wenqian Shen, Linglong Dai, Byonghyo Shim, Zhaocheng Wang, and Robert W. Heath. Channel feedback based on aod-adaptive subspace codebook in fdd massive mimo systems. *IEEE Transactions on Communications*, 66(11):5235–5248, 2018.
- [6] 3GPP. *NR; Physical layer procedures for data (Release 16)*. Technical Report TR 38.214. [Online] available: <http://www.3gpp.org>, 2020.
- [7] Haifan Yin and David Gesbert. A partial channel reciprocity-based codebook for wideband fdd massive mimo. *IEEE Transactions on Wireless Communications*, 21(9):7696–7710, 2022.
- [8] Christopher A. Metzler, Arian Maleki, and Richard G. Baraniuk. From denoising to compressed sensing. *IEEE Transactions on Information Theory*, 62(9):5117–5144, 2016.
- [9] Chengbo Li, Wotao Yin, and Yin Zhang. User’s guide for tval3: T_v minimization by augmented lagrangian and alternating direction algorithms. 2010.
- [10] Ping-Heng Kuo, H. T. Kung, and Pang-An Ting. Compressive sensing based channel feedback protocols for spatially-correlated massive antenna arrays. In *2012 IEEE Wireless Communications and Networking Conference (WCNC)*, pages 492–497, 2012.
- [11] An Liu, Vincent K. N. Lau, and Wei Dai. Exploiting burst-sparsity in massive mimo with partial channel support information. *IEEE Transactions on Wireless Communications*, 15(11):7820–7830, 2016.
- [12] Chao-Kai Wen, Wan-Ting Shih, and Shi Jin. Deep learning for massive mimo csi feedback. *IEEE Wireless Communications Letters*, 7(5):748–751, 2018.
- [13] Yaodong Cui, Aihuang Guo, and Chunlin Song. Transnet: Full attention network for csi feedback in fdd massive mimo system. *IEEE Wireless Communications Letters*, 11(5):903–907, 2022.
- [14] Sijie Ji and Mo Li. Clnet: Complex input lightweight neural network designed for massive mimo csi feedback. *IEEE Wireless Communications Letters*, 10(10):2318–2322, 2021.
- [15] Zhilin Lu, Jintao Wang, and Jian Song. Multi-resolution csi feedback with deep learning in massive mimo system. In *ICC 2020 - 2020 IEEE International Conference on Communications (ICC)*, pages 1–6, 2020.
- [16] Jie Wang, Guan Gui, Tomoaki Ohtsuki, Bamidele Adebisi, Haris Gacanin, and Hikmet Sari. Compressive sampled csi feedback method based on deep learning for fdd massive mimo systems. *IEEE Transactions on Communications*, 69(9):5873–5885, 2021.
- [17] Jiajia Guo, Chao-Kai Wen, Shi Jin, and Geoffrey Ye Li. Convolutional neural network-based multiple-rate compressive sensing for massive mimo csi feedback: Design, simulation, and analysis. *IEEE Transactions on Wireless Communications*, 19(4):2827–2840, 2020.
- [18] Dong Jin Ji and Byung Chang Chung. Concrete feedback layers: Variable-length, bit-level csi feedback optimization for fdd wireless communication systems. *IEEE Transactions on Wireless Communications*, 23(10):15353–15366, 2024.
- [19] Dong Jin Ji and Byung Chang Chung. Transformer-based efficient csi feedback for the band fdd mimo systems. *IEEE Wireless Communications Letters*, 13(2):343–346, 2024.
- [20] Vukan Ninkovic, Dejan Vukobratovic, Christian HÄger, Henk Wymeersch, and Alexandre Graell i Amat. Rateless autoencoder codes: Trading off decoding delay and reliability. In *ICC 2023 - IEEE International Conference on Communications*, pages 6361–6366, 2023.
- [21] Meilin Li, Wei Xu, Zhixiang Hu, and An Liu. A wideband csi feedback scheme based on loewner interpolation and model order reduction. *IEEE Wireless Communications Letters*, 14(11):3749–3753, 2025.
- [22] Omar El Ayach, Sridhar Rajagopal, Shadi Abu-Surra, Zhouyue Pi, and Robert W. Heath. Spatially sparse precoding in millimeter wave mimo systems. *IEEE Transactions on Wireless Communications*, 13(3):1499–1513, 2014.
- [23] Sanda Lefteriu and Athanasios C. Antoulas. Modeling multi-port systems from frequency response data via tangential interpolation. In *2009 IEEE Workshop on Signal Propagation on Interconnects*, pages 1–4, 2009.
- [24] A.J. Mayo and A.C. Antoulas. A framework for the solution of the generalized realization problem. *Linear Algebra and its Applications*, 425(2):634–662, 2007. Special Issue in honor of Paul Fuhrmann.
- [25] Peter Benner, Stefano Grivet-Talocia, Alfio Quarteroni, Gianluigi Rozza, Wil Schilders, and Luís Miguel Silveira. *System-and data-driven methods and algorithms*. De Gruyter, 2021.
- [26] Yuanzhe Wang, Chi-Un Lei, Grantham K. H. Pang, and Ngai Wong. Mfti: Matrix-format tangential interpolation for modeling multi-port systems. In *Design Automation Conference*, pages 683–686, 2010.
- [27] 3GPP. *Study on channel model for frequencies from 0.5 to 100 GHz (Release 16)*. Technical Report TR 38.901, available: <http://www.3gpp.org>, 2020.